Reduction of turbulent skin-friction drag by passively rotating discs - supplementary material

Paolo Olivucci[1], Daniel J. Wise[2] and Pierre Ricco[1]†

[1]Department of Mechanical Engineering, The University of Sheffield, S1 3JD Sheffield, United Kingdom

[2]Department of Fluid Dynamics, A*Star Institute of High Performance Computing, Singapore

(Received xx; revised xx; accepted xx)

This supplementary material presents further results that are used in the main paper.

S1. Estimation of the skin-friction drag reduction by Koch & Kozulovic (2013, 2014)

We discuss the procedure adopted by KK13 and KK14 to estimate the turbulent drag reduction on the surface of their passively spinning discs, shown in figure 1. KK13 and KK14 carried out seven experiments in a closed-circuit wind tunnel. The main flow parameters and results are summarized in table S1.

Although KK13 and KK14 measured the streamwise velocity profiles on and downstream of the disc, the wall-shear stress on the disc surface was not measured directly. They measured f^*, the average number of revolutions per second of the disc, and derived the spatial distribution of the streamwise slip length by assuming that the disc angular was constant, i.e., $u_s^*(z^*) = 2\pi f^* z^*$, where z^* is the spanwise distance from the disc center. It was further assumed that the 99% boundary-layer thickness δ_{99}^* over the disc was identical to the fixed-wall case. The boundary-layer thickness was measured experimentally at three spanwise distances from the disc centre and was in good agreement with the fixed-wall value, supporting the assumption. The wall-shear stress τ_w^* on the disc surface was estimated by modifying correlations for the skin-friction coefficient and the boundary-layer thickness, valid in the fixed-wall case:

$$\tau_w^*(x^*, z^*) = 0.0225\rho^*\nu^{*1/4}\frac{[U_\infty^* - u_s^*(z^*)]^{7/4}}{\delta_{99}(x^*)^{1/4}}, \tag{S1.1}$$

$$\delta_{99}^*(x^*) = 0.37(x^* - x_v^*)\left[\frac{\nu^*}{U_\infty^*(x^* - x_v^*)}\right]^{1/5}, \tag{S1.2}$$

where U_∞^* is the free-stream velocity, ν^* is the kinematic viscosity of air, and x_v^* is the virtual origin of the turbulent boundary layer, calculated by upstream extrapolation of the downstream measurements of δ_{99}^*. The spatial distribution of the reduction of the wall-shear stress, $\mathcal{R}_{xz}$, is obtained by use of (S1.1) with and without the local slip velocity u_s^*:

$$\mathcal{R}_{xz}(\%) = 100\left[1 - \left(1 - \frac{u_s^*}{U_\infty^*}\right)^{7/4}\right]. \tag{S1.3}$$

† Email address for correspondence: p.ricco@sheffield.ac.uk

Table S1: Flow parameters and results of the boundary-layer experiments from KK13 and KK14.

U^*_∞ [m/s]	δ^*_{99} [mm]	f^* [1/s]	Re_τ	D^+	$\overline{W}^+$	$U^+_{s,D}$	$\mathcal{R}_d(\%)$
20.32	3.98	9.94	276	6943	3.00	1.27	11.2
25.38	3.80	14.33	322	8481	3.54	1.50	12.6
30.41	3.67	19.01	366	9980	3.99	1.69	13.9
35.6	3.55	23.78	409	11500	4.33	1.84	14.7
40.7	3.46	28.78	449	12973	4.65	1.97	15.6
45.86	3.38	34.04	488	14444	4.94	2.09	16.3
50.96	3.31	39.04	525	15882	5.15	2.19	17.1

The spatially-averaged drag reduction over the half disc, $\mathcal{R}_d$, is computed by numerically integrating (S1.3) for our friction Reynolds number Re_τ=180. The result is shown in figure 12.

S2. Modelling of torques below the disc surface

The modelling of the torques given by the ball bearing and by the fluid friction in the housing cavity is presented.

S2.1. *Torque produced by the ball bearing*

Each disc is supported by a ball bearing fixed onto its shaft, as shown in dark grey in figure 3. The resisting torque T_b of a rolling-element bearing is caused by a combination of phenomena, such as lubrication, material deformation, thermal losses, and others. Its complete modelling is complex and the industrial estimates are usually performed through the use of empirical formulas (Harris & Kotzalas 2006). The main contribution to T_b is the load-induced rolling friction arising from the pressure contact between the rotary elements and the metal grooves, often named races. The interaction is similar to that experienced by train wheels on rail tracks.

Our estimate of T_b is based on the empirical formulas provided by a manufacturer of rolling-element bearings, the Swedish company SKF (`www.skf.com`). A realistic bearing model must be selected by considering the water-channel flow presented in table 1. The critical aspect is the capability of the bearing to support the axial load of the weight of the disc without generating a high-friction torque. Watertight seals are often used to protect the lubricant, but they are not modelled in our case because lubrication is not required for our slowly rotating and lightly loaded bearings.

A sound choice is a SKF angular-contact thrust bearing belonging to the series 7009. These bearings produce small friction under high axial loads and are available in sizes that are compatible with the required design. Using the bearing data-sheet parameters and an axial load corresponding to the weight of a disc of diameter $D = 5$, the SKF formulas return a friction torque that, translated into our outer units, is $|T_b| = 0.0001$. The effect of the axial load can be neglected because the weight of the disc is negligible. The use of a bearing torque that does not depend on W is justified because, at our slow rotation rates, only rolling friction occurs, which is nearly independent of the angular velocity. The bearing torque is therefore modelled as $T_b = |T_b|\mathrm{sgn}(W)$. The sign of the disc-tip velocity is accounted for because the friction of the bearing opposes the rotation.

S2.2. *Torque produced by the fluid friction in the housing cavity*

The motion of the fluid within the cavity under a disc results in a resisting torque T_h acting on the bottom surface of the disc. Two predictive models for T_h are used, thus avoiding the full simulation of the cavity flow.

We consider an idealized case where the disc angular velocity fluctuates following a monochromatic sinusoidal wave of zero mean and frequency f^*. We assume that the scaled frequency is small, i.e., $d_h^*\sqrt{f^*/\nu^*} \ll 1$, in order to model the cavity flow in a quasi-steady regime (a similar definition for a different oscillating-flow configuration is found in Barenghi & Jones 1989). In the case of full discs, shown in figure 2a, the discs fluctuate randomly, i.e., the time history of the disc motion shows a continuous frequency spectrum. The quasi-steadiness assumption is valid in all the cases because a large fraction of the disc kinetic energy corresponds to a range of frequencies f^* of the spectrum for which $d_h^*\sqrt{f^*/\nu^*} \ll 1$. In the half-disc cases, shown in figure 2b, the discs rotate with a finite mean angular velocity and thus the quasi-steadiness assumption is also always verified due to the standard deviation of the velocity fluctuations being much smaller than their temporal average. A further assumption is that the flow in the cavity is laminar. The steady flow between two coaxial infinite discs, one at rest and the other one moving with constant angular velocity Ω, was studied by Stewartson (1953) in the laminar regime at small and moderate Reynolds numbers. The azimuthal velocity u_θ is independent of the other two components, $u_\theta = r\Omega y_h/d_h$, where y_h is the wall-normal coordinate within the cavity and r is the radial coordinate with origin at the centre of the disc. The resisting torque is:

$$T_h = \frac{\pi D^4}{32 d_h Re_p}\Omega. \tag{S2.1}$$

We also model the flow in the cavity through the swirling boundary-layer solution of von Kármán (1921) for the flow induced by a disc beneath a semi-infinite fluid. The torque of the von-Kármán solution reads:

$$T_h = \mathrm{sgn}(\Omega)\frac{\pi G D^4}{32 Re_p^{1/2}}|\Omega|^{3/2}, \tag{S2.2}$$

where $G = 0.6159$ is a numerically-determined constant.

The most rigorous method to check the validity of the assumptions would be to carry out a DNS simulation of the cavity flow for each case, from which the scaled frequency parameter can be computed and the mean profiles and the resisting torque can be checked against the predictive model. This approach was not pursued because it is too computationally demanding. Future work should certainly be directed at improving the predictive model of the resisting cavity torque, mainly in view of quantitative comparisons with experimental data. Additional factors that will have to be modelled include the viscous shear stresses on the shaft supporting the disc, the secondary flows inside the cavity due to the ball bearing and the uneven steps or gaps, such as those of the experimental set-up shown in figure 1, and the effects of the transitional and turbulent flows inside the cavity at large angular velocities. The fluid friction below the disc could be minimized by designing the disc housing to be air filled, thus sealed from the turbulent flow of water on top of the disc.

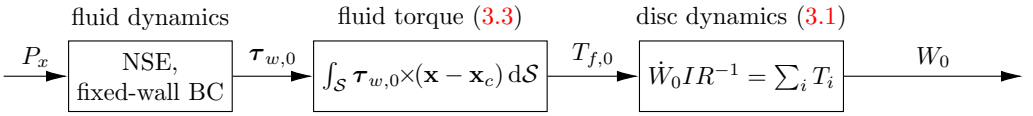

Figure S1: Block-diagram of the uncoupled disc-fluid system.

S3. Uncoupled dynamics of the full discs

S3.1. *Modelling of the uncoupled dynamics of the full discs*

The full-disc configuration is also studied under the simplifying assumption that the disc-tip velocity W is small. This assumption is reasonable as verified by the two-way-coupling simulations. In this uncoupled system, the torque engendered by the wall turbulence causes the motion of the discs, but the disc-tip velocity is so small that the wall turbulence is unaffected by the disc rotation. It is therefore a one-way coupling system, where the NSE are subject to the no-slip stationary-wall boundary conditions. Figure S1 depicts the uncoupled system, where there is no feedback from the disc to the fluid boundary conditions. The wall-shear-stress torque on the disc is first computed using the reference fixed-wall turbulent channel flow, and then the torque determines the disc dynamics.

The uncoupled system is obtained by a regular perturbation expansion for small W. We define the small parameter $\epsilon = \max_t [W^*(t^*)]/U_p^* \ll 1$ and we further assume that $W/T_f = \mathcal{O}(1)$, which is also reasonable because the instantaneous torque, $T_f \ll 1$, is given by the statistically homogeneous wall-shear stress acting over a disc without a preferential angular direction. We first expand the disc velocity as $W(t) = \epsilon W_0^m(t) + \mathcal{O}(\epsilon^2)$ (where $W_0^m = W^*/\max_t[W^*] = \mathcal{O}(1)$), the fluid velocity and pressure as $(\boldsymbol{u}, p)(\mathbf{x}, t; W) = (\boldsymbol{u_0}, p_0)(\mathbf{x}, t) + \epsilon(\boldsymbol{u_1}, p_1)(\mathbf{x}, t) + \mathcal{O}(\epsilon^2)$, the wall-shear stress as $\boldsymbol{\tau_w}(\mathbf{x}, t; W) = \boldsymbol{\tau_{w,0}}(\mathbf{x}, t) + \epsilon\boldsymbol{\tau_{w,1}}(\mathbf{x}, t) + \mathcal{O}(\epsilon^2)$, and the torque as $T_f(t; W) = \epsilon T_{f,0}^m(t) + \epsilon^2 T_{f,1}^m(t) + \mathcal{O}(\epsilon^2)$. (The subscript "0" henceforth indicates quantities that refer to the uncoupled case.) By substituting these expansions into (2.1), (2.2), (3.1), and (3.2), one finds that $\boldsymbol{u_0}$ satisfies the reference fixed-wall NSE equations at leading order and that, at the next order $\mathcal{O}(\epsilon)$, the disc-tip velocity W_0^m satisfies the dynamical equation driven by the fixed-wall torque $T_{f,0}^m$. At this next order, $\boldsymbol{u_1}$ satisfies linearized NSE equations, where the convection is driven by $\boldsymbol{u_0}$ and the wall boundary conditions synthesize the effect of the disc rotation on the fluid motion. We do not solve for $\boldsymbol{u_1}$ as we are interested in the leading-order behaviour. The feedback loop thus vanishes as the leading-order expansion leads to the no-slip stationary-wall boundary conditions.

The uncoupled model has a number of advantages over the coupled model. First, the uncoupled results can be compared to those from the coupled simulations, assessing the impact of the two-way coupling on the disc dynamics and the fluid flow. Second, in the uncoupled case, the equation of motion of the disc is linear because the torque is a known function of the turbulent flow. Therefore, the system is more easily studied in the frequency domain and the linearity of the disc equation of motion allows the explicit calculation of the frequency response of the disc dynamics to the fluid torque. Third, contrary to the coupled case, it is not required to perform new simulations for cases with discs of different diameter, but it is sufficient to simulate the fixed-wall channel flow once and then, from this flow, extract the fluid torques exerted on the disc-shaped patches of choice. This approach allows the study of a large number of cases: we have considered seventy diameters in the range $D^+ = 20 - 1200$.

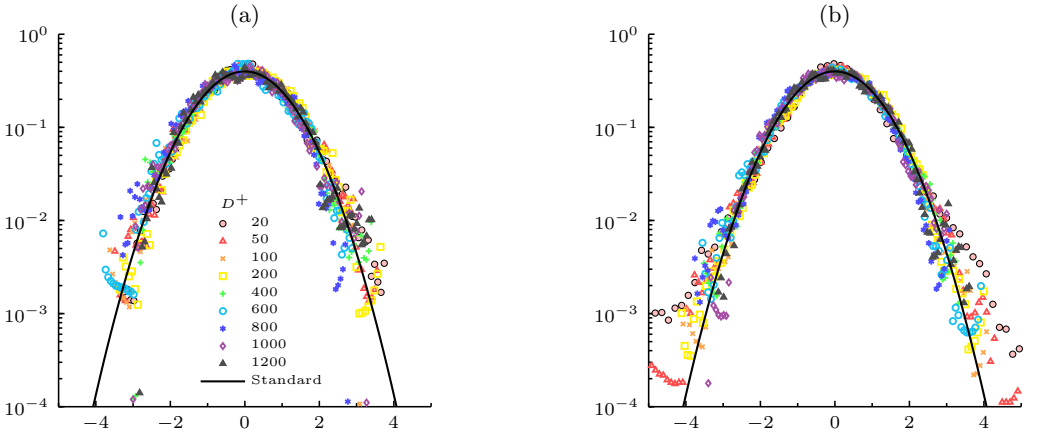

Figure S2: Standardized histogram plots of (a) W_0 and (b) $T_{f,0}$ for uncoupled-dynamics simulations. The solid line denotes the standard normal distribution.

S3.2. *Uncoupled dynamics in the physical domain*

This section discusses the uncoupled disc-fluid dynamics, represented schematically in the block-diagram of figure S1. The dynamics is still described by (4.1), but it becomes linear in the limit of small W because the torque $T_{f,0}$ is given by the fixed-wall reference flow. The solution to the uncoupled (4.1) is

$$W_0(t) = \frac{16\mathrm{e}^{-C_h t}}{\pi b \rho_d D^3} \int_0^t \left[T_{f,0}\left(\hat{t}\right) - T_b\right] \mathrm{e}^{C_h \hat{t}}\, \mathrm{d}\hat{t}, \tag{S3.1}$$

where $C_h = (Re_p d_h b \rho_d)^{-1}$ and $W_0(t=0) = 0$.

The red symbols in figure 7 show that $W_{0,\mathrm{rms}}$ behaves qualitatively as W_{rms} in the coupled-dynamics case, i.e., it decays as $D^{-0.7}$ after the maximum response for $D^+ = 100$. The fixed-wall fluid torque $T_{f,0}$ also follows a similar behaviour to the coupled case. The dependence of $T_{f,0}$ on D in the large-D range matches that of the coupled case, i.e., it also grows as $D^{2.2}$. The values of $W_{0,\mathrm{rms}}$ and $T_{f,0,\mathrm{rms}}$ are up to three times larger than in the coupled case, regardless of D. This result proves that the two-way interaction between the disc and the fluid produces an attenuating effect on the disc velocity and the torque.

The time evolutions of the fluid torque components $T^x_{f,0}$ and $T^z_{f,0}$ for the uncoupled case are shown in figure 9a (bottom). Differently from the coupled case, where the torque components are strongly anti-correlated, there is no noticeable correlation between $T^x_{f,0}$ and $T^z_{f,0}$. The contributions of the components of equation (4.2) to $\mathrm{Var}(T_{f,0})$ for the uncoupled case are presented in figure 9b by the blue symbols. Similar to the coupled simulations, the streamwise component of the torque dominates over the other two components. The magnitudes of the variance $\overline{T^{z2}_{f,0}}$ and covariance $\overline{T^x_{f,0} T^z_{f,0}}$ are much smaller than in the coupled simulations.

Figure S2 shows the standardized histograms of W_0 and $T_{f,0}$. The coupling has a negligible effect on the trends as the W_0 values follow the normal distribution for all the diameters and the heavy-tail behaviour of $T_{f,0}$ deviates from the normal curve at small diameters by a similar amount as in the coupled case.

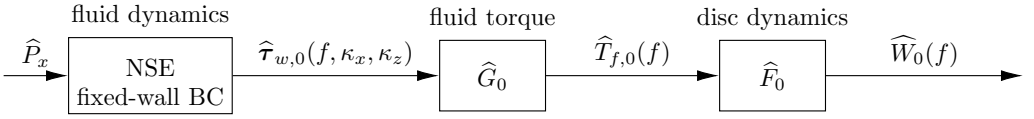

Figure S3: Block-diagram of the uncoupled disc-fluid system in the wavenumber-frequency domain, where $\widehat{\boldsymbol{\tau}}_{w,0}(\kappa_x,\kappa_z,f)$ is the wavenumber-frequency spectrum of the wall-shear stress, κ_x and κ_z are the streamwise and spanwise wavenumbers, f is the frequency, and the hat indicates the Fourier transform. $\widehat{G}_0$ and $\widehat{F}_0$ are the Fourier transforms of the fluid-torque integral (3.3) and the disc dynamical equation (4.1), respectively.

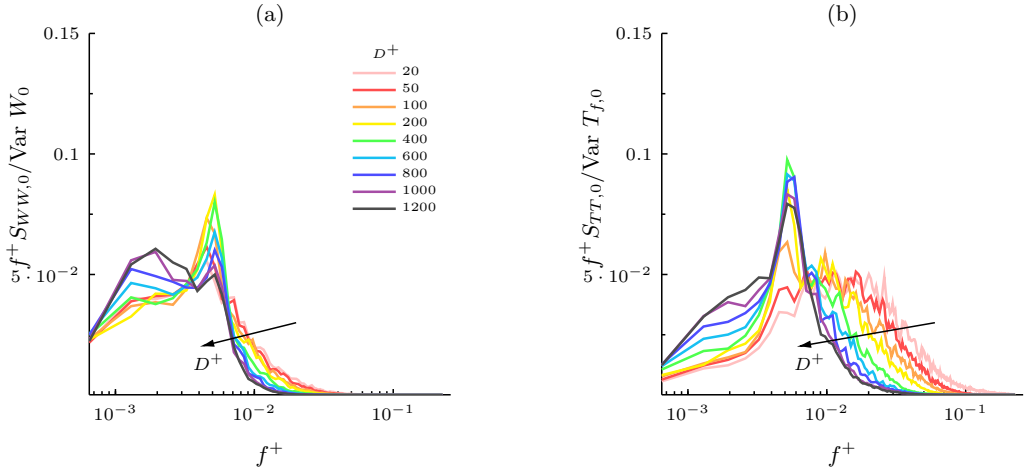

Figure S4: Power spectral densities, denoted by S with subscripts indicating the quantity and shown in pre-multiplied form. (a) Disc-tip velocity W_0 and (b) fluid torque $T_{f,0}$, computed from uncoupled-dynamics simulations. The plots are normalized with the total power.

S3.3. *Uncoupled dynamics in the frequency domain*

The dynamics of the full discs for small W is also investigated in the frequency domain, as shown in figure S3. As the response functions are difficult to study in the nonlinear coupled case, we focus on the linear uncoupled system.

The normalized PSDs of the disc-tip velocity and the fluid torque are displayed in figure S4. The PSDs of W_0 also follow an analogous behaviour to the coupled case, with the lower frequencies contributing more to the total power as D increases. Similar to the coupled case, the trends shift to low frequencies as the diameter increases and both quantities show the peak at about f^+=0.005. These maxima are now much more distinct than in the coupled case and the energy distribution of $T_{f,0}$ at higher frequencies is flatter.

The frequency-domain solution of (3.1) is:

$$\widehat{W}_0 = \frac{16}{\pi b \rho_s D^3 (2\pi i f + C_h)} \widehat{T_{f,0}}, \tag{S3.2}$$

where we have excluded T_b because $T_b \ll T_{h,0}$, revealing the scaling with D^{-3} and the inverse dependence on b and ρ_s, i.e., a thinner disc or a lighter material result in

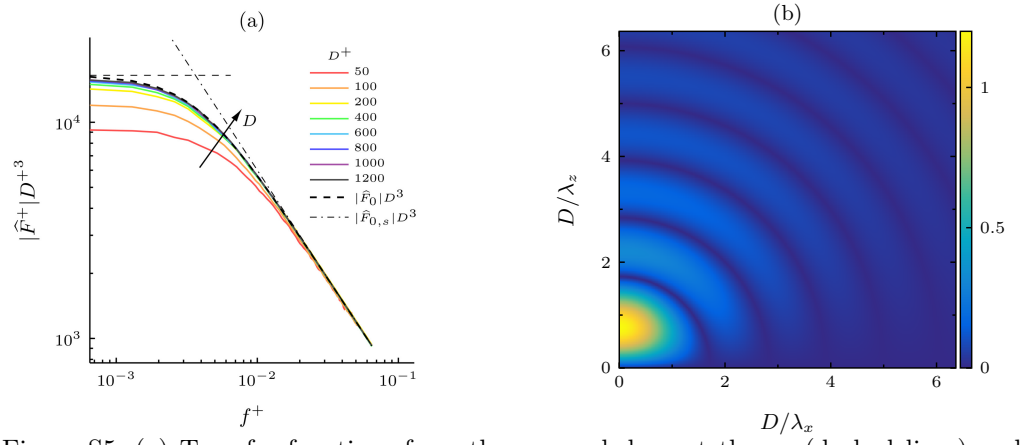

Figure S5: (a) Transfer functions from the uncoupled exact theory (dashed lines) and calculated from the coupled DNS simulations (solid lines). (b) Colour map plot of $|\Psi_R^x|$ as a function of the inverse of the streamwise and spanwise wavelengths, normalized with the disc diameter. This choice of coordinates emphasizes how the relative scale of the shear-stress wavelengths to the disc size affects the filtering properties of Ψ_R^x.

larger W. Equation (S3.2) can be written as $\widehat{F}_0 = \widehat{W}_0/\widehat{T_{f,0}}$, so that the gain is $|\widehat{F}_0| = 16/\pi b\rho_s D^3\sqrt{4\pi^2 f^2 + C_h^2}$. By neglecting friction to extract information about inertia, $|\widehat{F}_{0,s}| = 16/\pi b\rho_s D^3 2\pi f$. Figure S5 depicts the scaled $|\widehat{F}|$. When computed from the coupled nonlinear simulations, the procedure is not rigorous, but it offers a tool to assess whether the model is valid. The dashed lines show the matching with the inertia-driven behaviour for large frequencies $\sim f^{-1}$ and the constant behaviour at low frequencies, dictated by the housing-torque viscous effects. We find $\widehat{F}_0 \geqslant \widehat{F}$ at any f, with the difference reducing as $D^{-0.8}$ as D increases.

To study $\widehat{G}_0$, shown in figure S3, we neglect the dependence of $T_{f,0}$ on time and study its variance using temporally uncorrelated realizations $T_{f,0}(t_i)$, where the t_i are sufficiently delayed. We study the x-component $T_{f,0}^x$, given in (3.3) (the analysis is analogous for $T_{f,0}^z$), i.e.,

$$T_{f,0}^x(t_i;R) = \int_{\mathcal{S}} z\mathcal{F}_{xz}^{-1}\{\widehat{\tau}_{w,x,0}\}(\kappa_x,\kappa_z)\}\mathrm{d}x\mathrm{d}z = \tag{S3.3}$$

$$= \iint_{\mathbb{R}^2} \widehat{\tau}_{w,x,0}(\kappa_x,\kappa_z)\left(\frac{1}{4\pi^2}\int_{\mathcal{S}} z\mathrm{e}^{i\kappa_x x}\mathrm{e}^{i\kappa_z z}\mathrm{d}x\mathrm{d}z\right)\mathrm{d}\kappa_x\mathrm{d}\kappa_z \tag{S3.4}$$

$$= \iint_{\mathbb{R}^2} \widehat{\tau}_{w,x,0}\Psi_R^x\,\mathrm{d}\kappa_x\mathrm{d}\kappa_z, \tag{S3.5}$$

where $\mathcal{S}$ is the disc surface, $\widehat{\tau}_{w,x,0}$ is the spatial Fourier transform of $\tau_{w,x,0}(x,z)$, and $\mathcal{F}_{xz}^{-1}\{\cdot\}$ is its inverse. The function $\Psi_R^x(\kappa_x,\kappa_z)$ simplifies to:

$$\Psi_R^x(\kappa_x,\kappa_z) = R^3\Psi(R\kappa_x, R\kappa_z), \tag{S3.6}$$

where Ψ is

$$\Psi(\kappa_1,\kappa_2) = \frac{1}{2\pi^2\kappa_1}\int_{-1}^{1} z\sin\left(\kappa_1\sqrt{1-z^2}\right)\mathrm{e}^{i\kappa_2 z}\mathrm{d}z. \tag{S3.7}$$

We then study the magnitudes $|\widehat{\tau}_{w,x,0}|$ and $|\Psi_R^x|$ as the largest contribution to $\mathrm{Var}(T_{f,0}^x)$. The phase spectra Φ_τ and Φ_ψ also contribute to $\mathrm{Var}(T_{f,0}^x)$. The fixed-channel simulation data render Φ_τ a function with a uniformly distributed random phase. The function Φ_ψ

takes discrete values of either $-\pi/2$ or $\pi/2$, the sign being dictated by the same radial period observed for the oscillations of $|\Psi_R^x|$.

Figure S5b shows the magnitude $|\Psi_R^x|$ of the spectral filter function, calculated by solving the integral in (S3.7) numerically. The axes use the reciprocal of the wavelength (i.e., $1/\lambda_x{=}\kappa_x/2\pi$) normalized with the disc diameter to visualize the filtering behaviour of Ψ_R^x relative to the disc size. As the function $|\Psi_R^x|$ is even with respect to both wavenumbers, only the first quadrant is shown. A series of regularly-spaced oscillations can be observed, centred at the origin and decreasing in intensity at higher values of the diameter-wavelength ratio. The period of these oscillations, calculated along a radial direction centred at the origin, is $D/\lambda{=}1$ where $\lambda = \sqrt{\lambda_x^2 + \lambda_z^2}$, which means that $|\Psi_R^x|$ privileges spanwise modes, gradually decreasing at low spanwise wavenumbers and vanishing completely for purely streamwise modes. The maximum of $|\Psi_R^x|$ is determined to be a purely spanwise mode such that $D/\lambda_z = 0.732$. The largest individual contribution to the torque is given by the spanwise mode of $\tau_{w,x,0}$ whose wavelength is 1.37 times the diameter.

When observed in the absolute coordinates $1/\lambda_x$ and $1/\lambda_z$, the map of figure S5b corresponds to the case $D = 1$. When the disc size increases for $D > 1$, the coordinates scale linearly with D, which means that the maximum of $|\Psi_R^x|$ moves closer to $\kappa_z = 0$ and the radial wavelength of the oscillations decreases linearly, visually generating a "shrinking" effect centred at the origin. Similarly, when $D < 1$, $|\Psi_R^x|$ undergoes an "expansion" according to the same proportionality of the coordinates to D. The other effect of varying the disc size is that $|\Psi_R^x|$ is uniformly amplified by a factor of R^3, according to (S3.6). Larger discs therefore produce a very intense, localized filtering near the origin, while smaller discs have a weaker, spread-out filtering across a broad range of wavenumbers.

The PSD of the streamwise wall-shear stress reveals where the contributions to $|\widehat{\tau}_{w,x,0}|$ are located on average (not shown). It is found that, as $|\Psi_R^x|$ decreases and spreads out for increasingly large D, the entire shear-stress PSD attenuates, leading to smaller torque values. Conversely, for sufficiently small D, Ψ_R^x has an amplifying effect, with the most amplified modes being those of small streamwise wavenumbers, which correspond to the energy-containing region of the shear-stress PSD. Therefore, increasingly intense values of the torque occur as the disc size increases. This result qualitatively corresponds to that observed in figure 7, the precise dependence on D being determined by the specific form of the shear-stress spectrum.

As discussed in §4, the spanwise shear-stress torque T_f^z is much smaller than the streamwise one. A relation analogous to (S3.5) is derived for T_f^z:

$$T_{f,0}^z(R) = \iint_{\mathbb{R}^2} \widehat{\tau_{w,z,0}} \Psi_R^z \, \mathrm{d}\kappa_x \mathrm{d}\kappa_z. \tag{S3.8}$$

The difference between the spanwise filter function and the streamwise case is that $\Psi_R^z(\kappa_x, \kappa_z) = R^3\Psi(R\kappa_z, R\kappa_x)$, i.e., the spanwise and the streamwise wavenumbers are exchanged. This result can be shown by substituting z with x in (S3.5) and calculating the spatial integral. As implied by its definition, Ψ_R^z privileges streamwise modes of $\widehat{\tau_{w,z,0}}$ (as opposed to spanwise for Ψ_R^z) and its maximum amplification happens for the purely streamwise mode such that $D/\lambda_x \approx 0.732$.

The variance of $T_{f,0}$ is calculated by evaluating the variance of the right-hand side of (S3.5) and (S3.8) over the ensemble of uncorrelated shear-stress fields produced from the numerical simulation of the fixed-wall channel. After taking the square root, the resulting curve, measured directly from the spatial wall shear-stress fields through (3.3)

and shown in figure S5b alongside $T_{f,0,\mathrm{rms}}(D)$, shows excellent quantitative agreement with the numerical data.

It is conjectured that the change of slope occurring at around D^+=100 in figure 7 originates from the scaling behaviour of the filter-function kernel Ψ_R^x with respect to D. According to (S3.6) and the visualization shown in figure S5b, Ψ_R^x has two possible mechanisms for amplifying the wall-shear-stress modes. First, its amplitude grows as D^3 and, second, its maxima move relative to the wall-shear-stress spectrum maximum because the coordinates scale with D. While the first mechanism always results in an uniformly increasing amplification, the effect of the second mechanism is significant only when the Ψ_R^x maximum overlaps the region of maximum energy concentration of the wall-shear stress. On the contrary, if the Ψ_R^x maximum overlaps modes for which the wall-shear-stress PSD is zero, no local amplification takes place and those modes do not contribute to the integral (S3.5). Therefore, as D increases and the Ψ_R^x maximum moves closer to the origin, initially a regime is expected where both the first and the second mechanisms work in favour of the amplification because the kernel maximum moves progressively closer to the PSD maximum, until the two overlap. Thereafter, a regime of reduced amplification rate, i.e., a gentler slope of the $T_{f,\mathrm{rms}}(D)$ curve, is expected because the two maxima move apart. The diameter D_c at which the maximum of $|\Psi_R^x|$ and the maximum of $S_{\tau\tau}$ overlap can be used as an estimate of the slope-changing diameter. It is found that the maximum of $S_{\tau\tau}$ is located at around $1/\lambda_z = 1.2$, which implies that D_c=0.732/1.2=0.61 or $D_c^+ \approx 110$ in viscous units. This value matches the slope-changing point of $T_{f,0,\mathrm{rms}}(D)$ well, qualitatively endorsing the conjectured mechanism.

REFERENCES

Barenghi, C. F. & Jones, C. A. 1989 Modulated Taylor–Couette flow. *J. Fluid Mech.* **208**, 127–160.

Harris, T. A. & Kotzalas, M. N. 2006 *Essential Concepts of Bearing Technology*. CRC Press.

von Kármán, T. 1921 Über laminare und turbulente Reibung. *Z. Angew. Math. Mech.* **1** (4), 233–252.

Koch, H. & Kozulovic, D. 2013 Drag reduction by boundary layer control with passively moving wall. In *ASME 2013 Fluids Engineering Division Summer Meeting*, pp. V01BT15A004–V01BT15A004. American Society of Mechanical Engineers.

Koch, H. & Kozulovic, D. 2014 Influence of geometry variations on the boundary layer control with a passively moving wall. In *AIAA SciTech Forum, 52nd Aero. Sc. Meeting*, p. 0401.

Stewartson, K. 1953 On the flow between two rotating coaxial disks. *Math. Proc. Cambridge Phil. Soci.* **49** (2), 333–341.